symmetry

MDPI

Article

Transport Model Approach to Λ and $\bar{\Lambda}$ Polarization in Heavy-Ion Collisions

Larissa V. Bravina [1], Kyrill A. Bugaev [2,3], Oleksandr Vitiuk [4] and Evgeny E. Zabrodin [1,5,*]

[1] Department of Physics, University of Oslo, PB 1048 Blindern, N-0316 Oslo, Norway; larissa.bravina@fys.uio.no
[2] Bogolyubov Institute for Theoretical Physics, Metrologichna str. 14-B, UA-03680 Kiev, Ukraine; bugaev@fias.uni-frankfurt.de
[3] Faculty of Physics, Taras Shevchenko National University of Kyiv, UA-03022 Kiev, Ukraine
[4] Institute for Nuclear Research, National Academy of Sciences of Ukraine, Prospekt Nauki av. 47, UA-03680 Kiev, Ukraine; oleksandr.vitiuk@fys.uio.no
[5] Skobeltsyn Institute of Nuclear Physics, Moscow State University, RU-119991 Moscow, Russia
* Correspondence: zabrodin@fys.uio.no

Abstract: This paper investigates the symmetry breaking between the polarizations of Λ and $\bar{\Lambda}$ hyperons in relativistic collisions of heavy ions at intermediate and low energies. The microscopic transport model UrQMD is employed to study the thermal vorticity of hot and dense nuclear matter formed in non-central Au + Au collisions at center-of-mass energies $7.7 \leq \sqrt{s_{NN}} \leq 62.4$ GeV. The whole volume of an expanding fireball is subdivided into small cubic cells. Then, we trace the final Λ and $\bar{\Lambda}$ hyperons back to their last interaction point within a certain cell. Extracting the bulk parameters, such as energy density, net baryon density, and net strangeness of the hot and dense medium in the cell, one can obtain the cell temperature and the chemical potentials at the time of the hyperon emission. To do this, the extracted characteristics have to be fitted to the statistical model (SM) of ideal hadron gas. After that, the vorticity of nuclear matter and polarization of both hyperons are calculated. We found that the polarization of both Λ and $\bar{\Lambda}$ increases with decreasing energy of heavy-ion collisions. The stronger polarization of $\bar{\Lambda}$ is explained by (i) the slightly different freeze-out conditions of both hyperons and (ii) the different space–time distributions of Λ and $\bar{\Lambda}$.

Keywords: relativistic heavy-ion collisions; transport models; thermal vorticity; polarization of hyperons

Citation: Bravina, L.V.; Bugaev, K.A.; Vitiuk, O.; Zabrodin, E.E. Transport Model Approach to Λ and $\bar{\Lambda}$ Polarization in Heavy-Ion Collisions. *Symmetry* **2021**, *13*, 1852. https://doi.org/10.3390/sym13101852

Academic Editors: Vitaly Bornyakov, Konstantin Klimenko, Natalia Kolomoyets, Roman Rogalyov and Roman Zhokhov

Received: 1 July 2021
Accepted: 3 August 2021
Published: 3 October 2021

1. Introduction

Experiments with ultrarelativistic heavy-ion collisions at energies of the Relativistic Heavy Ion Collider (RHIC) (up to $\sqrt{s} = 200$ GeV) and the Large Hadron Collider (LHC) ($\sqrt{s} = 2.76$ and 5.02 TeV) have already provided a lot of information about the properties of a new state of matter: quark–gluon plasma (QGP). For the present statuses of theoretical and experimental studies, see [1] and the references therein. The transition between the QGP and hadronic matter in this range of energy densities and low baryon chemical potentials, however, appears to be a smooth crossover rather than the first order phase transition, expected at lower energies. This circumstance explains the rising interest in heavy-ion collisions at intermediate and low energies. At present, experiments are being carried out within the beam energy scan (BES) program at RHIC ($7.7 \leq \sqrt{s} \leq 200$ GeV) and at SPS CERN ($10 \leq E_{lab} \leq 160$ AGeV), and are being planned at new facilities, which are under construction, such as the Nuclotron-based Ion Collider fAcility (NICA) at JINR ($4 \leq \sqrt{s} \leq 11$ GeV) and the Facility for Antiproton and Ion Research (FAIR) at GSI ($2.7 \leq \sqrt{s} \leq 4.9$ GeV). In addition, slightly lower energy heavy-ion collisions at $2.3 \leq \sqrt{s} \leq 2.6$ GeV and $2.3 \leq \sqrt{s} \leq 3.5$ GeV are being measured by experiment HADES at GSI and BMN at JINR, respectively.

One of the ideas for studying properties of hot and dense matter is to employ, somehow, extremely high vorticity in noncentral heavy-ion collisions. It was suggested [2] that highly rotated partonic fluid should influence the polarization of hyperons, especially Λ and $\bar{\Lambda}$. This topic has become a popular branch of research in heavy-ion collisions—see, e.g., [3–10]—despite the fact that the polarization of both Λ and $\bar{\Lambda}$, measured by STAR Collaboration in Au + Au collisions at $\sqrt{s} = 200$ GeV, was found to be consistent with zero [11]. Recall that a similar result was obtained by ALICE Collaboration for Λ and $\bar{\Lambda}$ polarization in noncentral lead–lead collisions at $\sqrt{s} = 2.76$ TeV and 5.02 TeV [12]. Interest in the polarization phenomenon has significantly increased after the STAR Collaboration reported data [13] showing the nonzero polarization of both Λ and $\bar{\Lambda}$ in semi-peripheral gold–gold collisions at center-of-mass energies between 7.7 GeV and 200 GeV. It was shown that, being consistent with zero at $\sqrt{s} = 200$ GeV, hyperon polarization steadily increases to 2% with reducing c.m. energy to $\sqrt{s} = 7.7$ GeV. This observation has initiated a lot of new studies; see, e.g., [14–26] for review. However, the really puzzling fact was that the polarization of $\bar{\Lambda}$ at $\sqrt{s} > 7.7$ GeV was a bit larger, although consistent within the error bars with that of Λ. However, at $\sqrt{s} = 7.7$ GeV it suddenly rose up to $8.3 \pm 3\%$ [13]. It is quite difficult to explain this difference within the kinetic or hydrodynamic approaches, where the polarization of Lambdas and anti-Lambdas is nearly the same; see [10,17,18,22]. For instance, one can rely on the anomalous mechanism based on the axial vortical effect [15,16,25], or employ the interaction between the hyperon spins and the vorticity of the baryon current [21].

In [23], it was mentioned that the difference in polarizations of Λ and $\bar{\Lambda}$ may arise because of the different distributions of both hyperon species in space and time and, therefore, their different freeze-out conditions. Here, we would like to clarify this statement. Thermal vorticity and its connection with hyperon polarization is sketched in Section 2. We employ the UrQMD model [27,28] to study the polarization of Λ and $\bar{\Lambda}$ in noncentral gold–gold collisions generated with the energies from $\sqrt{s} = 7.7$ GeV to 62.4 GeV. We trace each hyperon from the final state to its last interaction point, elastic or inelastic, in the fireball. After determination of the energy density, net baryon density and net strangeness density of the freeze-out area, the thermal model of ideal hadron gas is used to calculate temperature T, baryon chemical potential μ_{B}, and strangeness chemical potential μ_{S}. Features of the transport model and formalism of the calculation of thermodynamic characteristics are discussed in Section 3. Section 4 describes the results of our study. We argue that differences in freeze-out conditions and space–time distributions of Λ and $\bar{\Lambda}$ can lead to different polarizations of both types of hyperons at intermediate and low energy regions. Simply, different areas of the expanding system have different vorticities at different times, whereas space–time distributions of Λ and $\bar{\Lambda}$ within the fireball are not the same. This circumstance becomes especially perceptible when the collision energy is reduced. Finally, the conclusions are drawn in Section 5.

2. Thermal Vorticity and Hyperon Polarization

One of the most popular approaches to the vorticity problem in noncentral collisions of heavy ions relies on the assumption of the local thermal equilibrium in the system at particle freeze-out [7]. Nowadays, other scenarios employing the axial vortical effect [15] have also become quite popular. In our study, we follow thermal approach formulated in [7,17]. In a system of natural (or Planck) units, the thermal vorticity tensor reads as follows:

$$\varpi_{\mu\nu} = \frac{1}{2}\left(\partial_\nu \beta_\mu - \partial_\mu \beta_\nu\right) \quad (1)$$

$$\beta^{\mu(\nu)} = u^{\mu(\nu)}/T \quad (2)$$

where $u^{\mu(\nu)}$ is the hydrodynamic four-velocity and T is the local temperature. It is connected to the ensemble-averaged spin four-vector $S^{\mu}(x,p)$ of a hyperon via the following:

$$S^{\mu}(x,p) = -\frac{1}{8m}\epsilon^{\mu\nu\rho\sigma}p_{\nu}\varpi_{\rho\sigma}(x)\,, \tag{3}$$

where m is the hyperon mass, and $\epsilon^{\mu\nu\rho\sigma}$ is antisymmetric tensor. If the thermal vorticity is decomposed into the following space–time components,

$$\boldsymbol{\varpi}_T = (\varpi_{0x},\varpi_{0y},\varpi_{0z}) = \frac{1}{2}\left[\nabla\left(\frac{\gamma}{T}\right)+\partial_t\left(\frac{\gamma\mathbf{v}}{T}\right)\right], \tag{4}$$

$$\boldsymbol{\varpi}_S = (\varpi_{yz},\varpi_{zx},\varpi_{xy}) = \frac{1}{2}\nabla\times\left(\frac{\gamma\mathbf{v}}{T}\right), \tag{5}$$

then the space–time components of the spin vector are the following:

$$S^0(x,p) = \frac{1}{4m}\mathbf{p}\cdot\boldsymbol{\varpi}_S\,, \tag{6}$$

$$\mathbf{S}(x,p) = \frac{1}{4m}\left(E_p\boldsymbol{\varpi}_S+\mathbf{p}\times\boldsymbol{\varpi}_T\right), \tag{7}$$

containing the momentum of hyperon $\mathbf{p}$ and its energy $E_p=\sqrt{\mathbf{p}^2+m^2}$.

How is this spin vector connected to the particle polarization? First of all, one has to perform a Lorentz boost of the spin vector of, for example, Λ hyperon, measured in the experiment in its local rest frame $S^{*\mu}=(0,\mathbf{S}^*)$ to the center-of-mass frame of a heavy-ion collision as follows:

$$\mathbf{S}^*(x,p) = \mathbf{S}-\frac{\mathbf{p}\cdot\mathbf{S}}{E_p\left(m+E_p\right)}\mathbf{p}\,. \tag{8}$$

Performing the transport model calculations, one has to determine the average vector $\mathbf{S}^*$, where the average is taken of all N Λ hyperons emitted from the whole system as follows:

$$\langle\mathbf{S}^*\rangle = \frac{1}{N}\sum_{i=1}^{N}\mathbf{S}^*(x_i,p_i)\,. \tag{9}$$

The global polarization of Λ in non-central collisions, measured in the experiment, is [8] the projection of averaged spin $\langle\mathbf{S}^*\rangle$ onto the direction of global orbital angular momentum $\mathbf{J}$ as follows:

$$P = \frac{\langle\mathbf{S}^*\rangle\cdot\mathbf{J}}{|\langle\mathbf{S}^*\rangle||\mathbf{J}|}\,. \tag{10}$$

This scheme was used by the STAR Collaboration in [13].

3. Models at Our Disposal

3.1. UrQMD Model

For our study, we employ the well-known ultra-relativistic quantum molecular dynamics (UrQMD) model [27,28]. It was created for the description of hadronic *hh*, hadron–nucleus *hA* and nucleus–nucleus $A+A$ collisions at energies ranging from that of SIS to RHIC and LHC. Such a broad energy span implies application of several mechanisms for the description of particle production and interaction. At energies below 1–2 GeV, the interaction dynamics at the hadronic level can be treated in terms of the interactions between hadrons and their excited states—resonances. It is worth noting here that the table of hadrons implemented in UrQMD is quite rich. As independent degrees of freedom, it includes 32 meson and 55 baryon states, as well as their antiparticles and explicit isospin-projected states from the Particle Data Group (PDG) [29] with masses up to 2.25 GeV/c. At higher collision energies, the production of new particles takes place via formation and subsequent fragmentation of new colored objects, colloquially known as strings. Strings are uniformly stretched between quarks and antiquarks, or between

quarks and diquarks, or between their antistates. The string tension κ is constant and equals $\kappa \approx 1$ GeV/fm. The excited strings are fragmented into pieces via the Schwinger mechanism [30] of (di)quark-anti(di)quark pair production, and newly produced hadrons are assumed to be uniformly distributed in the rapidity space. In contrast to models based on the color-exchange scheme [31–34], UrQMD utilizes the longitudinal mechanism of string excitation [35]. In the latter case, the string masses arise from the momentum transfer. The model also employs tables of experimentally available information, such as widths of resonances, cross sections of hadronic interactions, and hadron decay modes. In the case of a lack of needed information, UrQMD relies on the one-boson exchange model, isospin symmetry conditions and detailed balance considerations. The propagation of particles is governed by Hamilton equations of motion. For the description of hA and $A + A$ collisions, the hadronic cascade is used. Note that, due to the uncertainty principle, newly produced hadrons can interact only after a certain period called the *formation time*. However, if hadrons contain the valence quarks, they can interact immediately with the reduced cross section $\sigma = \sigma_{qN}$. The Pauli principle is taken into account via the blocking of the final state if the outgoing phase space is occupied. Further details can be found elsewhere; see [27,28,36].

3.2. Statistical Model of Ideal Hadron Gas

From the description of basic features of the microscopic transport model UrQMD, it is obvious that conditions of the global or local thermal equilibrium are not explicitly implemented in it. One has to, therefore, develop the procedure to determine the thermodynamic characteristics of the system created in heavy-ion collisions. Relaxation of hot and dense nuclear matter produced in relativistic heavy-ion collisions to local chemical and thermal equilibrium within microscopic transport models was studied in [37–43]. In what follows, we employ the method suggested there to calculate both the temperature and chemical potentials of the hot and dense medium. Namely, the volume of the expanding fireball is subdivided into relatively small cells. To measure the energy density ε, net baryon density ρ_B, and net strangeness density ρ_S of each cell, we generate a sufficient number of heavy-ion collisions at the same center-of-mass energy and with the same centrality. If the mixture of hadron species is in local equilibrium, its properties are fully determined by the set of distribution functions as follows:

$$f(p, m_i) = \left\{ \exp\left(\frac{\epsilon_i - \mu_i}{T} \right) \pm 1 \right\}^{-1} \tag{11}$$

where we again use the system of natural units with $c = \hbar = k_B = 1$. In Equation (11), m is the mass, p is the momentum, $\epsilon_i = \sqrt{p^2 + m_i^2}$ is the energy, and μ_i is the chemical potential of the hadron species i, respectively. The sign $+$ stands for fermions and $-$ stands for bosons. Since the electric chemical potential is usually much smaller, compared to that of the baryon charge or strangeness, we will disregard it and consider only the baryon and strangeness chemical potentials as attributed to the conserved charges in strong interactions. Thus, the total chemical potential of the i-th hadron, possessing the baryon charge B and strange charge S, reads as follows:

$$\mu_i = B_i \mu_{\mathrm{B}} + S_i \mu_{\mathrm{S}} \tag{12}$$

Then, the particle number density n_i and the energy density ε_i within the volume V are calculated as the first and the second moments of the distribution function $f(p, m_i)$, respectively, as follows:

$$n_i \equiv \frac{N_i}{V} = \frac{g_i}{(2\pi)^3} \int f(p, m_i) d^3 p \tag{13}$$

$$\varepsilon_i \equiv \frac{E_i}{V} = \frac{g_i}{(2\pi)^3} \int \epsilon_i f(p, m_i) d^3 p \tag{14}$$

where g_i is the spin-isospin degeneracy factor. In order to obtain T, μ_B and μ_S one has to insert the extracted microscopic parameters $\{\varepsilon^{mic}, \rho_B^{mic}$ and $\rho_S^{mic}\}$ into the system of nonlinear equations as follows:

$$\varepsilon^{mic} = \sum_i \varepsilon_i(T, \mu_B, \mu_S) \,, \tag{15}$$

$$\rho_S^{mic} = \sum_i S_i \, n_i(T, \mu_B, \mu_S) \,, \tag{16}$$

$$\rho_B^{mic} = \sum_i B_i \, n_i(T, \mu_B, \mu_S) \,, \tag{17}$$

It is important to stress that the set of hadron species, employed in the statistical model as independent degrees of freedom, should be the same as that used by the microscopic model. A comparison of the hadron yields and energy spectra, given by the microscopic model, to the SM spectra in the central area of heavy-ion collisions reveals that hot and dense nuclear matter needs about 5–8 fm/c to reach the vicinity of the chemical and local equilibrium. The extracted macroscopic parameters help us to determine the freeze-out conditions of Λ and $\bar{\Lambda}$ hyperons, and temperature is employed further for calculation of the thermal vorticity of nuclear matter.

4. Vorticity, Freeze-Out and Hyperon Polarization

In the present paper, polarization of Λ and $\bar{\Lambda}$ is studied in noncentral Au + Au collisions at c.m. energies corresponding to the Beam Energy Scan program at RHIC, i.e., from $\sqrt{s} = 200$ GeV to 7.7 GeV. During the BES, experimental data were obtained by the STAR Collaboration for centrality bin $20\% \leq \sigma/\sigma_{geo} \leq 50\%$. To compare the model calculations with the data, we generated at each energy not less than one million collisions with the impact parameter (i) $b = 6$ fm and (ii) $b = 9$ fm, roughly corresponding to minimum and maximum centrality values of the selected bin. The number of events generated at each centrality is listed in Table 1. In addition, the imposed kinematic cuts on the hyperon spectra, $|y| \leq 1$ for the rapidity window and $0.1 \leq p_T \leq 3$ GeV/c for the transverse momentum correspond to those of the STAR experiment [13].

Table 1. Number of Au + Au collisions generated within UrQMD with impact parameters $b = 6$ fm and $b = 9$ fm at energies $\sqrt{s} = 7.7, 11.5, 14.5, 19.6, 27, 39,$ and 62.4 GeV.

$\sqrt{s}$ (GeV)	7.7	11.5	14.5	19.6	27	39	62.4
N_{events}, $b = 6$ fm (10^6)	1.4	1.3	1.2	1.1	1.0	1.0	1.0
N_{events}, $b = 9$ fm (10^6)	1.7	1.5	1.3	1.1	1.0	1.0	1.0

Before starting the study of vorticity and hyperon polarization, we have checked the conservation of angular momentum in the model. Recall that UrQMD implies explicit conservation of energy, momentum and charges, such as the electric charge, net baryon number and net strangeness, in every collision process. Angular momentum conservation, however, is not checked in the program. It can be calculated as follows:

$$\vec{J} = \sum_{i=1}^{N} [\vec{r}_i \times \vec{p}_i] \,, \tag{18}$$

where $\vec{r}_i$ and $\vec{p}_i$ are radius–vector and momentum of the i-th particle, respectively, and N is the total number of particles in the event. Calculations of J (in units of $\hbar$) for Au + Au collisions with $b = 6$ fm at four different energies are shown in Figure 1. One can see that total angular momentum is not exactly conserved, especially at the early stages of the collisions. We found that the violation occurs mainly due to the presence of inelastic collisions via decays of strings. On the other hand, maximum relative deviations do not

exceed $\simeq 2\%$, i.e., they are very small. Therefore, we concluded that angular momentum in UrQMD calculations is nearly conserved.

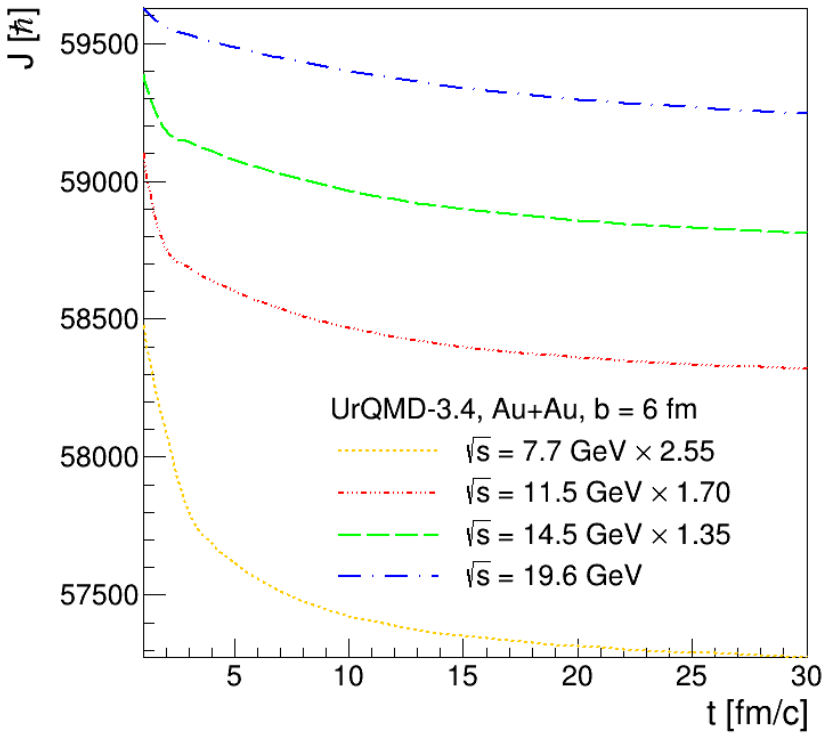

Figure 1. (Color online) Evolution of angular momentum in UrQMD generated Au + Au collisions with $b = 6$ fm at $\sqrt{s} = 7.7$ GeV (dotted curve), 11.5 GeV (dot-dashed curve), 14.5 GeV (dashed curve), and 19.6 GeV (dash-dotted curve). For better visualization, the first three distributions are multiplied by factors 2.55, 1.70, and 1.35, respectively.

Then, microscopic transport models usually favor non-uniform continuous freeze-out of hadrons [44–46] rather than the sudden freeze-out at given temperature or energy density, which is typical for the majority of hydrodynamic models. Figure 2 displays emission density dN/dt of Λ and $\bar{\Lambda}$ in gold–gold collisions with the impact parameter $b = 6$ fm generated at energies $\sqrt{s} = 7.7$ GeV and 62.4 GeV. Here, t corresponds to time after the beginning of nuclear collision when the particle has experienced its last elastic or inelastic scattering. Vertical arrows indicate the average emission times of both hyperons.

The emission of both hyperons during the first few fermis is small but rapidly increasing. The bulk production of Λ and $\bar{\Lambda}$ takes place between 10 and 25 fm/c, although both Λ and $\bar{\Lambda}$ are continuously emitted until the very late stage of the system evolution. Despite the qualitative similarity of Λ and $\bar{\Lambda}$ distributions, the mean values of the freeze-out times indicate that $\bar{\Lambda}$ hyperons are emitted, on average, earlier than Λ's. In addition, the lower the c.m. energy, the shorter the time of emission. For instance, the mean freeze-out time for (Λ and $\bar{\Lambda}$) equals 21.3 fm/c and 19.8 fm/c, respectively, at $\sqrt{s} = 7.7$ GeV. Such a small difference looks almost insignificant; however, one has to bear in mind that the system rapidly expands and, therefore, its temperature drops very quickly.

Thus, the macroscopic characteristics at the hyperon freeze-out, i.e., the temperatures and chemical potentials of the areas from where the hyperons are emitted, have to be investigated. To obtain this information, the whole volume of the fireball was subdivided into small cubic cells with volume $V = 1$ fm^3. Then, after the generation of a million collisions, we were able to calculate for each cell the time evolution of average total energy density ε, net baryon density $\rho_{\mathrm{B}} = \rho_B - \rho_{\bar{B}}$, and net strangeness density $\rho_{\mathrm{S}} = \rho_S - \rho_{\bar{S}}$. It is worth noting that the calculations were made in the local rest frame of the cell. The standard time step was chosen as $\Delta t = 1$ fm/c. Having this information at hand, one may

employ the procedure described in Section 3.2 to determine the temperature T and both chemical potentials, μ_B and μ_S, for each cell. Recall that, even in very central collisions with the impact parameter of $b = 0$ fm temperature, the baryon chemical potential and strangeness chemical potential are not distributed uniformly, even at midrapidity. This is illustrated in Figures 3–5, where distributions of calculated T, μ_B, μ_S are shown together with the values of $\varepsilon, \rho_B, \rho_S$ extracted from microscopic model calculations at three different time slices, namely $t = 10$ fm/c (Figure 3), $t = 16$ fm/c (Figure 4), and $t = 20$ fm/c (Figure 5) corresponding to the maximal hyperon production.

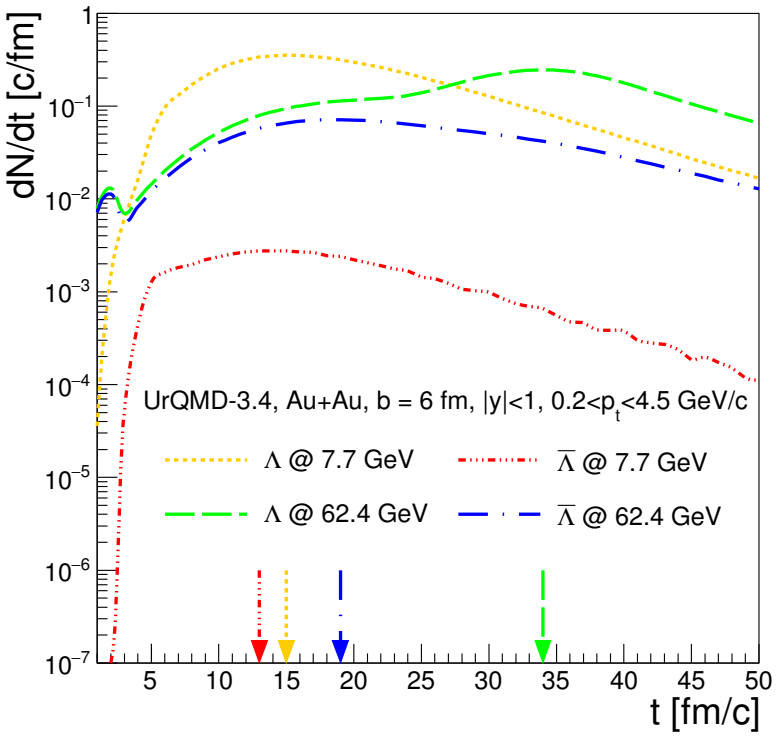

Figure 2. (Color online) Emission rates of Λ and $\bar{\Lambda}$ per unit time in UrQMD generated Au + Au collisions with $b = 6$ fm at $\sqrt{s} = 7.7$ GeV (dotted and dot-dashed curves) and 62.4 GeV (long-dashed and dash-dotted curves). Vertical arrows show the averaged emission time of the species.

It is easy to see in these three figures that spectators have the highest energy densities and highest temperatures among the other parts of the expanding fireball. Recall that this is the so-called proper temperature obtained in the local rest frame of each cell. The area between the spectators possesses the same temperature everywhere, except for the fireball surface, which is colder, compared to the inner area. Both chemical potentials are also almost uniform in the inner part of the system. This observation supports the hypothesis of the local equilibrium of nuclear matter produced in relativistic heavy-ion collisions. At late stages, the medium in the center of the fireball is quite dilute, and its temperature decreases; see Figure 5. The baryochemical potential in the central zone of the reaction demonstrates the opposite tendency. It is minimal in the spectator areas and maximal on the fireball surface. In contrast to the temperature, the baryon chemical potential is increasing in the central region when the matter here is becoming more dilute, as seen in Figures 4 and 5. On the other hand, the behavior of the chemical potential of strangeness is similar to that of the temperature. Therefore, the temperature of a cell from which the hadrons are emitted depends on both the time of the evolution and the position of the cell inside the fireball.

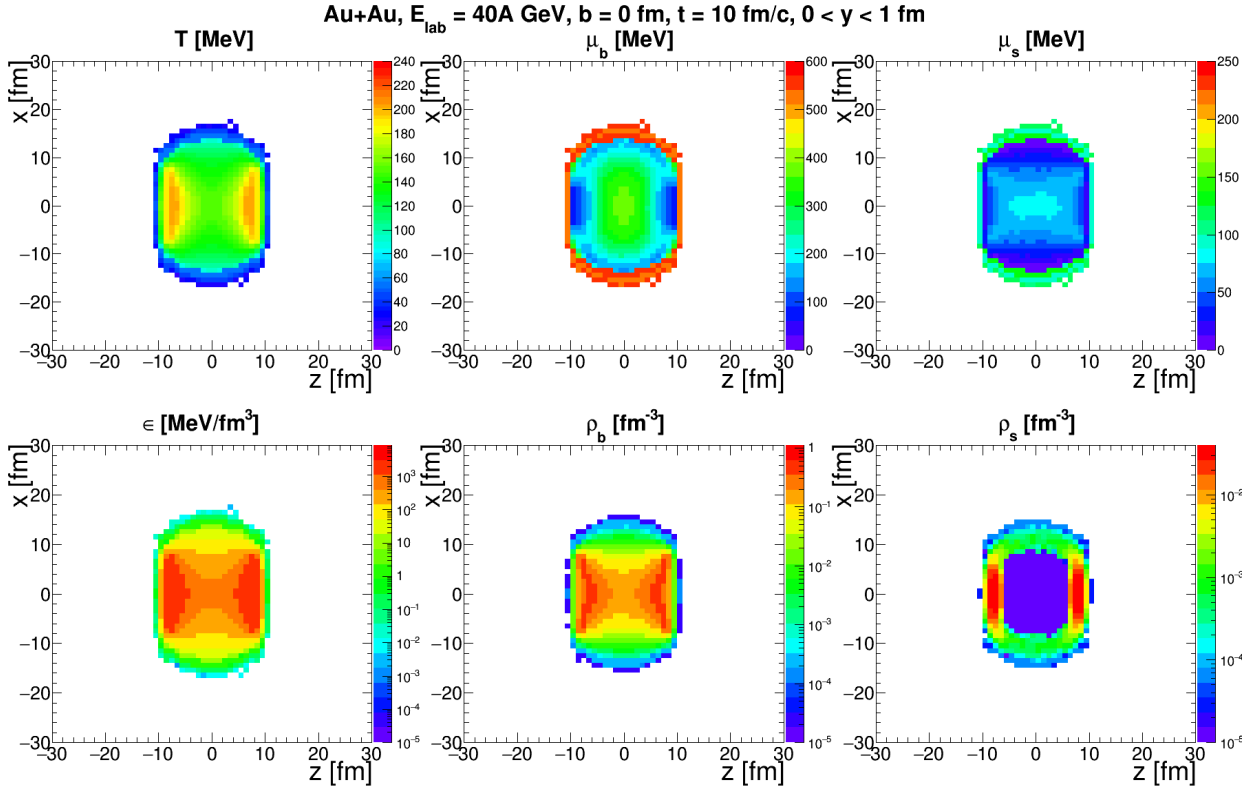

Figure 3. (Color online) **Upper** row: distribution of T, μ_B, μ_S at midrapidity $0 < y < 1$ in the reaction plane of central Au + Au collisions at $E_{lab} = 40$ AGeV ($\sqrt{s} = 8.7$ GeV) at time $t = 10$ fm/c. **Bottom** row: the same as upper row but for ε, ρ_B and ρ_S.

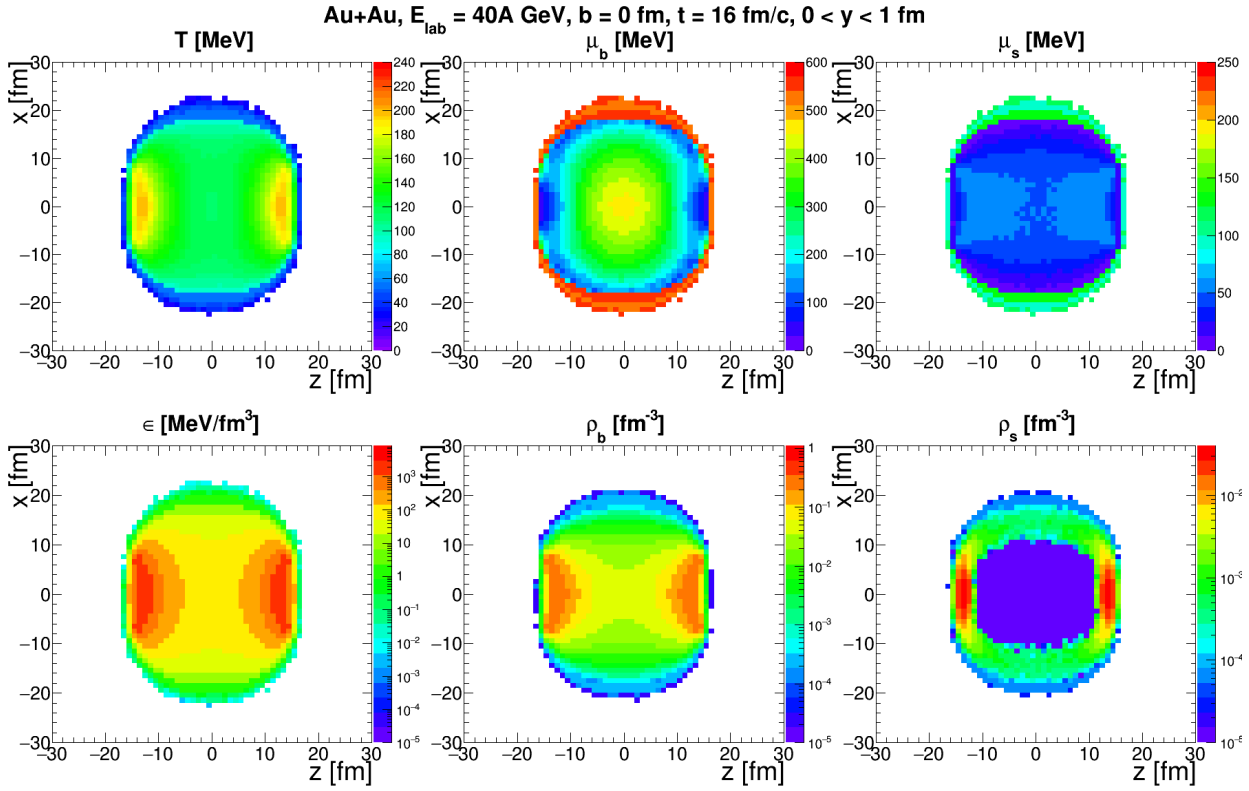

Figure 4. (Color online) The same as Figure 3 but for time $t = 16$ fm/c.

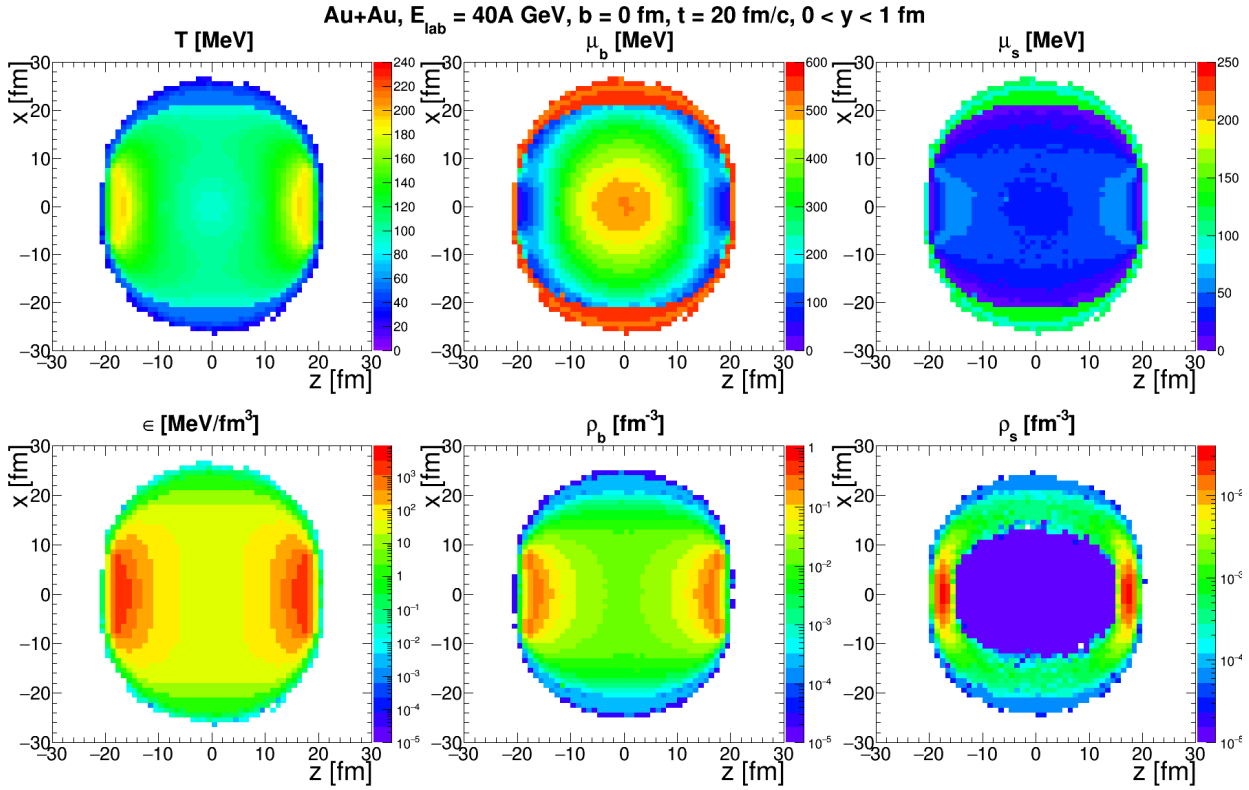

Figure 5. (Color online) The same as Figure 3 but for time $t = 20$ fm/c.

What about noncentral collisions? Let us pick up gold–gold collisions generated at $\sqrt{s} = 7.7$ GeV with the impact parameter $b = 6$ fm. Figure 6 presents the temperature distribution in the reaction plane of this reaction at time $t = 15$ fm/c.

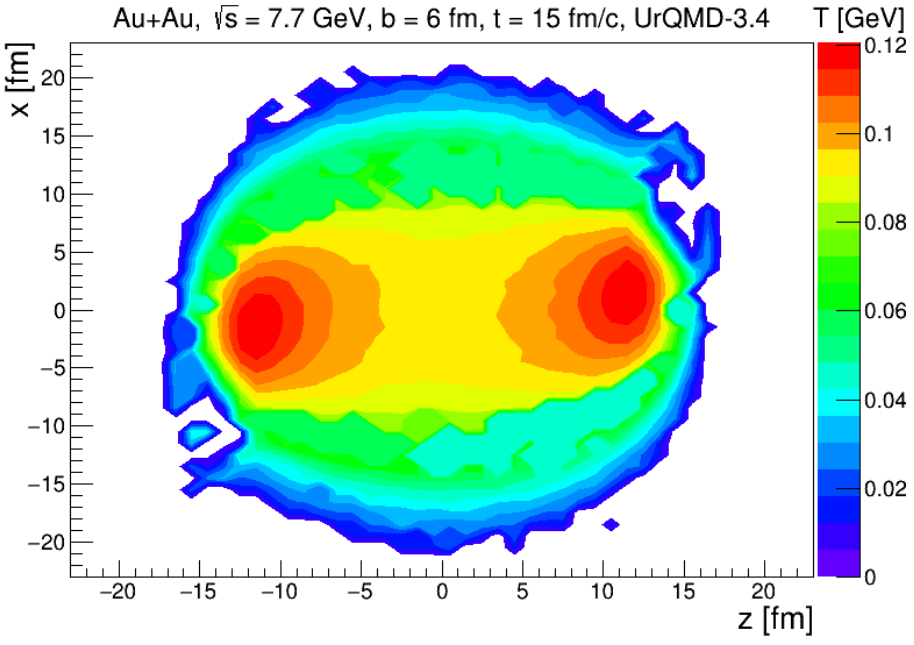

Figure 6. (Color online) Temperature distribution within the reaction plane of UrQMD-generated Au + Au collisions at $\sqrt{s} = 7.7$ GeV with $b = 6$ fm at time $t = 15$ fm/c.

Similar to very central collisions, the temperature in noncentral collisions is highest in the spectator zones and lowest at the surface of the expanding system. Therefore, it is important to investigate the spatial distributions of Λ and $\bar{\Lambda}$ hyperons in the whole volume. It appears that these distributions are different, as displayed in Figure 7. Here, the density distributions $d^2N/dxdz$ of Λ and $\bar{\Lambda}$ in the reaction plane of gold–gold collisions with $b = 6$ fm at $\sqrt{s} = 19.6$ GeV are shown at the moment $t = 15$ fm/c, together with the collective velocities of the cells. Lambdas have a maximum number density in the spectator areas, i.e., they follow the baryon-rich matter. Other Λs are distributed almost uniformly between these zones. In contrast, anti-Lambdas reach a maximum concentration in the baryon-less areas, although the total distribution of $\bar{\Lambda}$ looks more isotropic, compared to that of Λ. Therefore, in addition to slightly different average freeze-out times, both hyperons experience their last inelastic or elastic collision in different space areas. Knowing the collective velocity and temperature of each cell, one can determine the vorticity map of the system.

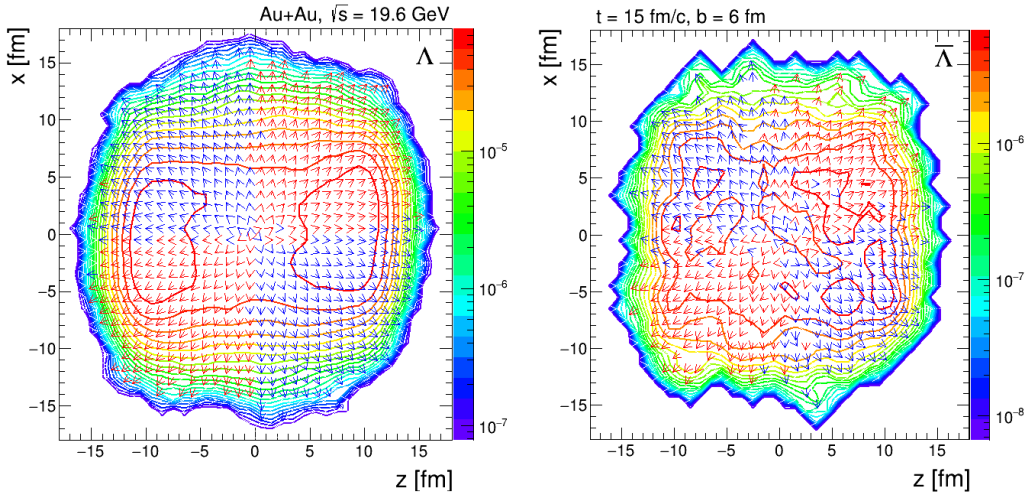

Figure 7. (Color online) Contour plots: density distributions $d^2N/dxdz$ of Λ (**left** window) and $\bar{\Lambda}$ (**right** window) in the reaction plane of UrQMD-calculated Au+Au collisions with impact parameter $b = 6$ fm at $\sqrt{s} = 19.6$ GeV at time $t = 15$ fm/c. Arrows indicate collective velocities of the cells.

We focus on the reaction-plane component ϖ_{zx}. The reason is simple: compared to the other two spatial vorticity components, the component ϖ_{zx} is directed along the angular momentum of the system. This circumstance makes it very important for the calculation of the polarization of both hyperons, Λ and $\bar{\Lambda}$. The vorticity component ϖ_{zx}, calculated in Au + Au with $b = 6$ fm at $\sqrt{s} = 7.7$ GeV at time $t = 15$ fm/c, is shown in Figure 8.

In this figure, one can distinctly see the violation of the quadruple structure of ϖ_{zx}. Recall that at c.m. energies above 19.6 GeV, the thermal vorticity in z–x plane of noncentral heavy ion collisions is well subseparated into four regions almost coinciding with the plane quadrants [8,22]. The matter in the first and third quadrants possesses a negative vorticity, whereas in the second and forth ones, its vorticity is positive. At lower collision energies, this picture is severely distorted by the emergence of the central region with a small but still negative vorticity. Therefore, the first and third quadrants with a negative thermal vorticity are not separated anymore; see Figure 8. This region increases with the decreasing energy of the collisions. Because of the expansion of the fireball, the strength of ϖ_{zx} decreases, though the average vorticity remains negative. The negative thermal vorticity results in the positive polarization of hyperons, in line with the other calculations [10].

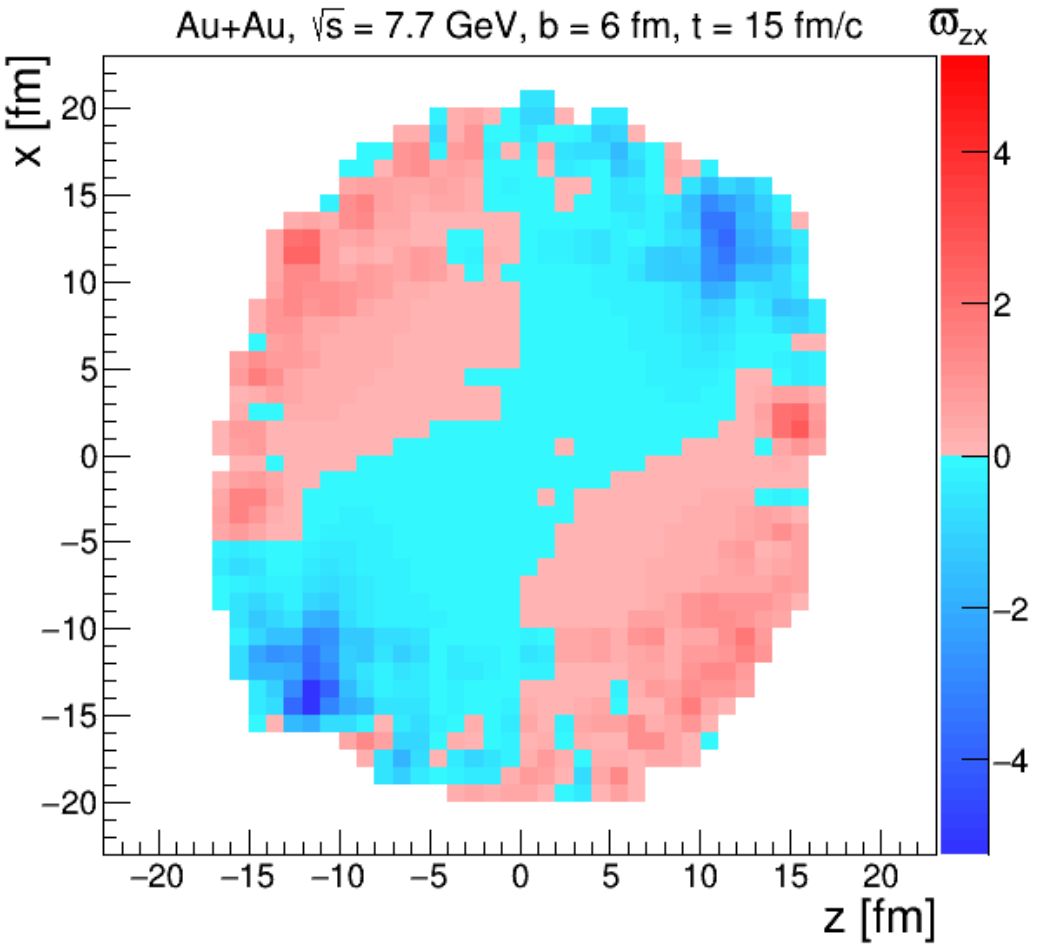

Figure 8. (Color online) Spatial component of thermal vorticity ϖ_{zx}, calculated within the reaction plane of UrQMD-generated Au + Au collisions with $b = 6$ fm at $\sqrt{s} = 7.7$ GeV and at $t = 15$ fm/c.

In transport models, we can trace back the trajectory of any particle to its last interaction point in the system. In the case of hyperons, we know both the hyperon momentum and the thermal vorticity of the cell from which it was emitted. Now, one can employ Equation (3) to calculate the global polarization of Λ and $\bar{\Lambda}$. The polarization of Λ hyperons emitted within the time span from 1 fm/c to 30 fm/c in Au + Au collisions with $b = 6$ fm generated at energies from $\sqrt{s} = 7.7$ GeV to 62.4 GeV is depicted in Figure 9 (left). The corresponding distributions for the evolution of polarization of $\bar{\Lambda}$ in these collisions are shown in Figure 9 (right). We can see that the polarization of both hyperon species, emitted at early times, is very high because the system of colliding nuclei possesses the largest vorticity at this moment. In the course of expansion of the fireball, its vorticity ϖ_{zx} rapidly drops and, therefore, the polarization of both Λ and $\bar{\Lambda}$, emitted at later times, also decreases. As one can see in Figure 2, anti-Lambdas are frozen slightly earlier than Lambdas. This circumstance leads to stronger global polarization of $\bar{\Lambda}$ compared to Λ. Note also that the difference in polarization of the hyperons emitted after $t \approx 15$ fm/c is very small. At lower energies of nuclear collisions, Λ and $\bar{\Lambda}$ are (i) frozen earlier and (ii) produced more abundantly in the areas with a negative vorticity. Both phenomena work toward increasing the global hyperon polarization.

The dependence of the global polarization of both hyperons on energy is is presented in Figure 10. Here, the UrQMD calculations of Au + Au collisions with impact parameters (i) $b = 6$ fm and (ii) $b = 9$ fm are compared to the STAR data [13,47]. The centrality range, therefore, is $20\% \leq \sigma/\sigma_{geo} \leq 45\%$ for UrQMD calculations and $20\% \leq \sigma/\sigma_{geo} \leq 50\%$ for the experimental data. Only hyperons emitted earlier than $t = 30$ fm/c are taken into

account. One can see that UrQMD reproduces the experimental very well for both Λ and $\bar{\Lambda}$ polarization for collisions with energy $\sqrt{s} = 11.6$ GeV or higher. The larger the impact parameter of the collision, the larger the hyperon polarization. The model correctly reproduces the fact that the polarization of $\bar{\Lambda}$ is stronger than that of Λ at energies below $\sqrt{s} = 62.4$ GeV.

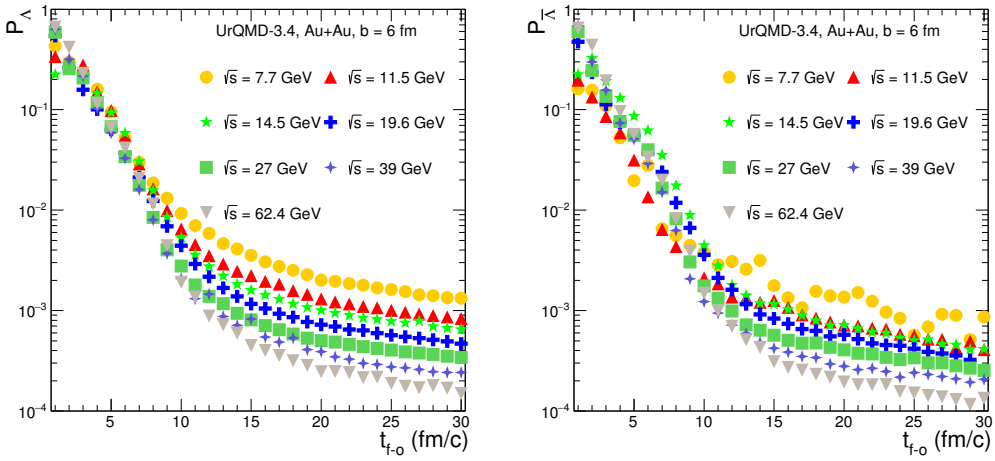

Figure 9. (Color online) Global polarization of Λ (**left** plot) and $\bar{\Lambda}$ (**right** plot) emitted at $1 \leq t \leq 30$ fm/c in UrQMD-calculated Au + Au collisions with $b = 6$ fm at energies $\sqrt{s} = 7.7$ GeV (circles), 11.5 GeV (triangles up), 14.5 GeV (stars), 19.6 GeV (crosses), 27 GeV (squares), 39 GeV (asterisks) and 62.4 GeV (triangles down), respectively.

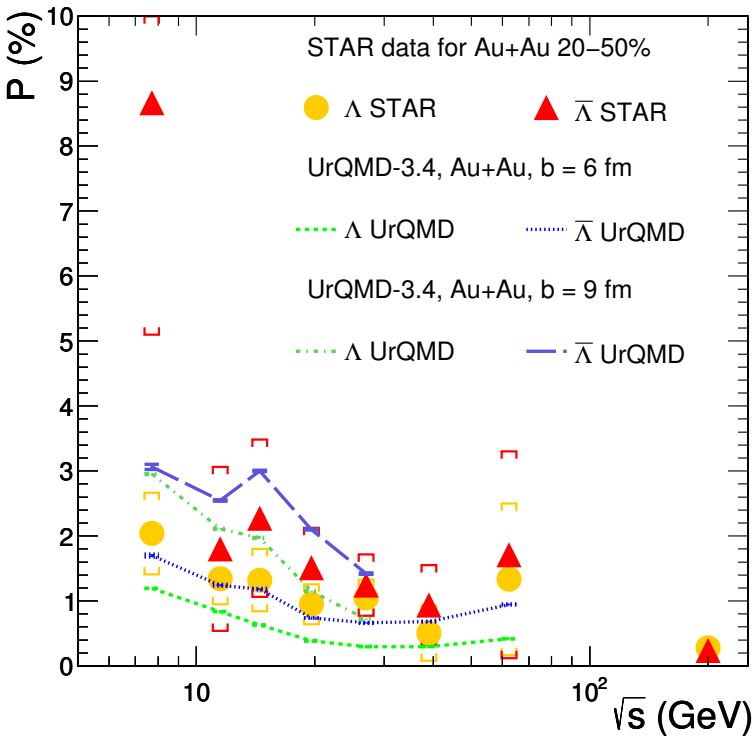

Figure 10. (Color online) Polarization of Λ and $\bar{\Lambda}$ in UrQMD-calculated Au + Au collisions with $b = 6$ fm and $b = 9$ fm at energies from $\sqrt{s} = 7.7$ GeV to 200 GeV. Results for Λ at $b = 6(9)$ fm are shown by a dashed (dash-dotted) line, whereas results for $\bar{\Lambda}$ at these centralities are depicted by a dotted (long-dashed) line, respectively. Symbols indicate the STAR data taken from [13,47]. Figure is taken from Ref. [23].

There is only one discrepancy in this plot, namely, the very strong global polarization of $\bar{\Lambda}$ measured at $\sqrt{s} = 7.7$ GeV is underpredicted by a factor of 2.5; see Figure 10. The effect may originate partly from the very low statistics for $\bar{\Lambda}$ at this energy range, thus resulting in large error bars. Therefore, the statistics of the experiment must be improved. If the large magnitude of $\bar{\Lambda}$ polarization is to be preserved in the case of increased statistics, one should consider further modifications of the approach. One of the possible ways is to slightly reduce the average freeze-out time for anti-Lambdas in the model. Other effects, such as the axial vortical effect and so forth, can be also added to the considered scheme. This extremely interesting problem should be clarified in the nearest future.

5. Conclusions

We studied the thermal vorticity of nuclear matter produced in noncentral gold–gold collisions at energies from $\sqrt{s} = 7.7$ GeV to 62.4 GeV, and connected to it the polarization of Λ and $\bar{\Lambda}$ hyperons in these collisions. The Au + Au collisions were generated within the UrQMD model with two impact parameters, $b = 6$ fm and $b = 9$ fm, roughly corresponding to the centrality region 20–50%, studied by the STAR Collaboration during the Beam Energy Scan program. The whole volume of the expanding system was subseparated into small cubic cells for better location of the areas from which both hyperon species were emitted. To obtain the temperatures of the individual cells, the statistical model of ideal hadron gas, containing precisely the same number of hadronic species as UrQMD, was employed. This allowed us to study the evolution of the reaction-plane component of thermal velocity, ϖ_{zx}.

Firstly, the freeze-out of Λ and $\bar{\Lambda}$ was checked. It was found that $\bar{\Lambda}$ are frozen, on average, slightly earlier, compared to Λ. Additionally, at high energies of heavy ion collisions, both Λ and $\bar{\Lambda}$ are distributed almost uniformly at midrapidity. At intermediate and lower energies, spectators are closer to the midrapidity range. The density of Λ reaches a maximum in the baryon-rich areas, whereas $\bar{\Lambda}$ are mainly distributed in the baryon-free zones. These areas of the fireball have different thermal vorticities; therefore, the global polarizations of Λ and $\bar{\Lambda}$ are also different. At higher energies, the polarizations of both hyperons at midrapidity are similar.

At lower energies, the thermal vorticity of matter decreases more slowly, compared to that at higher energies. Additionally, hyperons are produced more abundantly in the regions with a negative vorticity. This circumstance leads to positive polarization of both hyperon species. Our calculations are in a good agreement with the results of the STAR experiment, except the anomalously high value (though, with very large error bars) of $\bar{\Lambda}$ polarization in Au + Au collisions at $\sqrt{s} = 7.7$ GeV. This result needs further investigation.

Author Contributions: All authors contributed equally to this work. All authors have read and agreed to the published version of the manuscript.

Funding: The work was supported by the Norwegian Centre for International Cooperation in Education (SIU) under grants "CPEA-LT-2016/10094—From Strong Interacting Matter to Dark Matter" and "UTF-2016-long-term/10076—Training of Bachelor, Master and Ph.D. Students specialized in high energy physics". The work of L.V.B. and E.E.Z. was supported by the Norwegian Research Council (NFR) under grant No. 255253/F50—"CERN Heavy Ion Theory" and by the Russian Foundation for Basic Research (RFBR) under grants No. 18-02-40084 and 18-02-40085. K.A.B. and O.V. acknowledge a partial support from the program, "Participation in the novel international projects in high energy and nuclear physics", launched by the Section of Nuclear Physics and Energetics of NAS of Ukraine.

Institutional Review Board Statement: Not applicable.

Informed Consent Statement: Not applicable.

Data Availability Statement: Not applicable.

Acknowledgments: The fruitful discussions with L. P. Csernai, Yu. B. Ivanov and O. V. Teryaev are gratefully acknowledged.

Conflicts of Interest: The authors declare no conflict of interests.

References

1. Liu, F.; Wang, E.; Wang, X.-N.; Xu, N.; Zhang, B.-W. (Eds.) *Quark Matter Wuhan 2019*; Elsevier: Amsterdam, The Netherlands, 2021; Volume 1005.
2. Liang, Z.; Wang, X.-N. Globally polarized quark-gluon plasma in non-central A + A collisions. *Phys. Rev. Lett.* **2005**, *94*, 102301; Erratum in *Phys. Rev. Lett.* **2006**, *96*, 039901(E). [CrossRef]
3. Betz, B.; Gyulassy, M.; Torrieri, G. Polarization probes of vorticity in heavy ion collisions. *Phys. Rev. C* **2007**, *76*, 044901. [CrossRef]
4. Becattini, F.; Piccinini, F.; Rizzo, J. Angular momentum conservation in heavy ion collisions at very high energy. *Phys. Rev. C* **2008**, *77*, 024906. [CrossRef]
5. Rogachevsky, O.; Sorin, A.; Teryaev, O. Chiral vortaic effect and neutron asymmetries in heavy-ion collisions. *Phys. Rev. C* **2010**, *82*, 054910. [CrossRef]
6. Gao, J.H.; Liang, Z.-T.; Pu, S.; Wang, Q.; Wang, X.-N. Chiral anomaly and local polarization effect from the quantum kinetic approach. *Phys. Rev. Lett.* **2012**, *109*, 232301. [CrossRef]
7. Becattini, F.; Csernai, L.P.; Wang, D.J. Λ polarization in peripheral heavy ion collisions. *Phys. Rev. C* **2013**, *88*, 034905; Erratum in *Phys. Rev. C* **2016**, *93* 069901. [CrossRef]
8. Becattini, F.F.; Inghirami, G.; Rolando, V.; Beraudo, A.; Del Zanna, L.; De Pace, A.; Nardi, M.; Pagliara, G.; Chandra, V. A study of vorticity formation in high energy nuclear collisions. *Eur. Phys. J. C* **2015**, *75*, 406; Erratum in *Eur. Phys. J. C* **2018**, *78*, 354. [CrossRef]
9. Pang, L.G.; Petersen, H.; Wang, Q.; Wang, X.N. Vortical Fluid and Λ Spin Correlations in High-Energy Heavy-Ion Collisions. *Phys. Rev. Lett.* **2016**, *117*, 192301. [CrossRef] [PubMed]
10. Li, H.; Pang, L.G.; Wang, Q.; Xia, X.L. Global Λ polarization in heavy-ion collisions from a transport model. *Phys. Rev. C* **2017**, *96*, 054908. [CrossRef]
11. Abelev, B.; Aggarwal, M.M.; Ahammed, Z.; Anderson, B.D.; Arkhipkin, D.; Averichev, G.S.; Bai, Y.; Balewski, J.; Barannikova, O.; Barnby, L.; et al. Global polarization measurement in Au + Au collisions. *Phys. Rev. C* **2007**, *76*, 024915. [CrossRef]
12. Acharya, S.; Adamova, D.; Adhya, S.P.; Adler, A.; Adolfsson, J.; Aggarwal, M.M.; Rinella, G.A.; Agnello, M.; Agrawal, N.; Ahammed, Z.; et al. Global polarization of Λ and $\bar{\Lambda}$ hyperons in Pb-Pb collisions at the LHC. *Phys. Rev. C* **2020**, *101*, 044611. [CrossRef]
13. Adamczyk, L.; Adkins, J.K.; Agakishiev, G.; Aggarwal, M.M.; Ahammed, Z.; Ajitanand, N.N.; Alekseev, I.; Anderson, D.M.; Aoyama, R.; Aparin, A.; et al. Global Λ hyperon polarization in nuclear collisions: Evidence for the most vortical fluid. *Nature* **2017**, *548*, 62–65.
14. Becattini, F.; Karpenko, I.; Lisa, M.A.; Upsal, I.; Voloshin, S.A. Global hyperon polarization at local thermodynamic equilibrium with vorticity, magnetic field, and feed-down. *Phys. Rev. C* **2017**, *95*, 054902. [CrossRef]
15. Sorin, A.; Teryaev, O. Axial anomaly and energy dependence of hyperon polarization in heavy-ion collisions. *Phys. Rev. C* **2017**, *95*, 011902(R). [CrossRef]
16. Baznat, M.; Gudima, K.; Sorin, A.; Teryaev, O. Femto-vortex sheets and hyperon polarization in heavy-ion collisions. *Phys. Rev. C* **2016**, *93*, 031902. [CrossRef]
17. Xie, Y.; Wang, D.; Csernai, L.P. Global Λ polarization in high energy collisions. *Phys. Rev. C* **2017**, *95*, 031901. [CrossRef]
18. Karpenko, I.; Becattini, F. Study of Λ polarization in relativistic nuclear collisions at $\sqrt{s_{NN}} = 7.7$–200 GeV. *Eur. Phys. J. C* **2017**, *77*, 213. [CrossRef]
19. Ivanov, Y.B.; Soldatov, A.A. Vorticity in heavy-ion collisions at the JINR Nuclotron-based Ion Collider fAcility. *Phys. Rev. C* **2017**, *95*, 054915. [CrossRef]
20. Kolomeitsev, E.E.; Toneev, V.D.; Voronyuk, V. Vorticity and hyperon polarization at energies available at JINR Nuclotron-based Ion Collider fAcility. *Phys. Rev. C* **2018**, *97*, 064902. [CrossRef]
21. Csernai, L.P.; Kapusta, J.I.; Welle, T. Λ and $\bar{\Lambda}$ spin interaction with meson fields generated by the baryon current in high energy nuclear collisions. *Phys. Rev. C* **2019**, *99*, 021901. [CrossRef]
22. Ivanov, Y.B.; Toneev, V.D.; Soldatov, A.A. Estimates of hyperon polarization in heavy-ion collisions at collision energies $\sqrt{s_{NN}} = 4$–40 GeV. *Phys. Rev. C* **2019**, *100*, 014908. [CrossRef]
23. Vitiuk, O.; Bravina, L.V.; Zabrodin, E.E. Is different Λ and $\bar{\Lambda}$ polarization caused by different spatio-temporal freeze-out picture? *Phys. Lett. B* **2020**, *803*, 135298. [CrossRef]
24. Xie, Y.; Chen, G.; Csernai, L.P. A study of Λ and $\bar{\Lambda}$ polarization splitting by meson field in PICR hydrodynamic model. *Eur. Phys. J. C* **2021**, *81*, 12. [CrossRef]
25. Ivanov, Y.B. Global Λ polarization in moderately relativistic nuclear collisions. *Phys. Rev. C* **2021**, *103*, L031903. [CrossRef]
26. Becattini, F.; Lisa, M.A. Polarization and Vorticity in the Quark–Gluon Plasma. *Ann. Rev. Nucl. Part. Sci.* **2020**, *70*, 395–423. [CrossRef]
27. Bass, S.A.; Belkacem, M.; Bleicher, M. Microscopic models for ultrarelativistic heavy ion collisions. *Prog. Part. Nucl. Phys.* **1998**, *41*, 255–369. [CrossRef]
28. Bleicher, M.; Zabrodin, E.; Spieles, C.; Bass, S.; Ernst, C.; Soff, S.; Bravina, L.; Belkacem, M.; Weber, H.; Stöcker, H.; et al. Relativistic hadron hadron collisions in the ultrarelativistic quantum molecular dynamics model. *J. Phys. G* **1999**, *25*, 1859–1896. [CrossRef]
29. Tanabashi, M.; Hagiwara, K.; Hikasa, K.; Nakamura, K.; Sumino, Y.; Takahashi, F.; Tanaka, J.; Agashe, K.; Aielli, G.; Amsler, C.; et al. Particle Data Group. *Phys. Rev. D* **2018**, *98*, 030001. [CrossRef]

30. Schwinger, J. On Gauge Invariance and Vacuum Polarization. *Phys. Rev.* **1951**, *82*, 664–679. [CrossRef]
31. Drescher, H.J.; Ostapchenko, S.; Pierog, T.; Werner, K. Parton based Gribov-Regge theory. *Phys. Rep.* **2001**, *350*, 93–289. [CrossRef]
32. Amelin, N.S.; Bravina, L.V. The Monte Carlo Realization of Quark-Gluon String Model for Description of High-energy Hadron Hadron Interactions. *Sov. J. Nucl. Phys.* **1990**, *51*, 133–140.
33. Bleibel, J.; Bravina, L.V.; Zabrodin, E.E. How many of the scaling trends in *pp* collisions will be violated at $\sqrt{s_{NN}} = 14$ TeV?—Predictions from Monte Carlo quark-gluon string model. *Phys. Rev. D* **2016**, *93*, 114012. [CrossRef]
34. Ostapchenko, S. Monte Carlo treatment of hadronic interactions in enhanced Pomeron scheme: I. QGSJET-II model. *Phys. Rev. D* **2011**, *83*, 014018. [CrossRef]
35. Andersson, B.; Gustafson, G.; Ingelman, G.; Sjostrand, T. Parton Fragmentation and String Dynamics. *Phys. Rept.* **1983**, *97*, 31–145. [CrossRef]
36. Petersen, H.; Steinheimer, J.; Burau, G.; Bleicher, M.; Stocker, H. A Fully Integrated Transport Approach to Heavy Ion Reactions with an Intermediate Hydrodynamic Stage. *Phys. Rev. C* **2008**, *78*, 044901. [CrossRef]
37. Bravina, L.V.; Gorenstein, M.; Belkacem, M.; Bass, S.; Bleicher, M.; Brandstetter, M.; Hofmann, M.; Soff, S.; Spieles, C.; Weber, H.; et al. Local thermodynamical equilibrium and the equation of state of hot, dense matter created in Au + Au collisions at AGS. *Phys. Lett. B* **1998**, *434*, 379–387. [CrossRef]
38. Bravina, L.V.; Brandstetter, M.; Gorenstein, M.I.; Zabrodin, E.E.; Belkacem, M.; Bleicher, M.; Bass, S.; Ernst, C.; Hofmann, M.; Soff, S.; et al. Local thermal and chemical equilibration and the equation of state in relativistic heavy ion collisions. *J. Phys. G* **1999**, *25*, 351–362. [CrossRef]
39. Bravina, L.V.; Zabrodin, E.E.; Gorenstein, M.I.; Bass, S.; Belkacem, M.; Bleicher, M.; Brandstetter, M.; Ernst, C.; Hofmann, M.; Neise, L.; et al. Local equilibrium in heavy ion collisions: Microscopic model versus statistical model analysis. *Phys. Rev. C* **1999**, *60*, 024904. [CrossRef]
40. Bravina, L.V.; Zabrodin, E.E.; Bass, S.A.; Bleicher, M.; Brandstetter, M.; Faessler, A.; Fuchs, C.; Greiner, W.; Soff, S.; Stocker, H.; et al. Equation of state of resonance rich matter in the central cell in heavy ion collisions at $S^{1/2} = 200$ AGeV. *Phys. Rev. C* **2001**, *63*, 064902. [CrossRef]
41. Bravina, L.V.; Arsene, I.; Nilsson, M.S.; Tywoniuk, K.; Zabrodin, E.E.; Bleibel, J.; Faessler, A.; Fuchs, C.; Bleicher, M.; Burau, G.; et al. Microscopic models and effective equation of state in nuclear collisions in the vicinity of $E_lab = 30A$ GeV at the GSI Facility for Antiproton and Ion Research (FAIR) and beyond. *Phys. Rev. C* **2008**, *78*, 014907. [CrossRef]
42. Oliinychenko, D.; Petersen, H. Deviations of the Energy-Momentum Tensor from Equilibrium in the Initial State for Hydrodynamics from Transport Approaches. *Phys. Rev. C* **2016**, *93*, 034905. [CrossRef]
43. Somnath, D.; Sudipan, D.; Chattopadhyay, S. Thermalization of dense hadronic matter in Au + Au collisions at energies available at the Facility for Antiproton and Ion Research. *Phys. Rev. C* **2016**, *94*, 054901.
44. Bass, S.A.; Dumitru, A.; Bleicher, M.; Bravina, L.; Zabrodin, E.; Stocker, H.; Greiner, W. Hadronic freezeout following a first order hadronization phase transition in ultrarelativistic heavy ion collisions. *Phys. Rev. C* **1999**, *60*, 021902. [CrossRef]
45. Bravina, L.V.; Mishustin, I.; Amelin, N.; Bondorf, J.; Csernai, L. Freezeout in relativistic heavy ion collisions at AGS energies. *Phys. Lett. B* **1995**, *354*, 196–201. [CrossRef]
46. Bravina, L.V.; Mishustin, I.N.; Bondorf, J.P.; Faessler, A.; Zabrodin. E.E. Microscopic study of freezeout in relativistic heavy ion collisions at SPS energies. *Phys. Rev. C* **1999**, *60*, 044905. [CrossRef]
47. Adam, J.; Adamczyk, L.; Adams, J.R.; Adkins, J.K.; Agakishiev, G.; Aggarwal, M.M.; Ahammed, Z.; Ajitanand, N.N.; Alekseev, I.; Anderson, D.M.; et al. Global polarization of Λ hyperons in Au + Au collisions at $\sqrt{S_{NN}} = 200$ GeV. *Phys. Rev. C* **2018**, *98*, 014910. [CrossRef]